metals

MDPI

Article

Multi-Physics Coupling Parameter Analysis of TiZrHf Medium Entropy Alloy

Mengzhou Chang [1,2,*], Bo Wang [1], Chuang Chen [1] and Enling Tang [1]

[1] Key Laboratory of Transient Physical Mechanics and Energy Conversion Materials of Liaoning Province, Shenyang Ligong University, Shenyang 110159, China; wangbo260215@163.com (B.W.); chenchuang517@126.com (C.C.); tangenling0721@163.com (E.T.)
[2] School of Mechanical Engineering, Nanjing University of Science and Technology, Nanjing 210094, China
* Correspondence: changmengzhou@hrbeu.edu.cn

Abstract

The complex coupling relationships among the thermal, mechanical, and electrical physical parameters of TiZrHf-based medium-entropy alloys represent a key factor restricting their practical applications under complex extreme environments. In this study, the thermo-mechanical-electrical coupling characteristics of TiZrHf and $TiZrHfCu_{0.8}$ medium-entropy alloys were systematically investigated using a self-developed experimental platform. The results demonstrate that TiZrHf and $TiZrHfCu_{0.8}$ alloys exhibit elastoplastic and superelastic-plastic compressive deformation behaviors, respectively, with both elastic modulus and ultimate strength decreasing monotonically with increasing temperature T. Electrical property measurements reveal that the electrical resistivities ρ of the two alloys range from 3 to 35 $\times$ 10^{-6} Ω·m. Notably, $TiZrHfCu_{0.8}$ possesses a lower resistivity that is independent of the test frequency f. Moreover, ρ increases with T but decreases with applied stress σ. At a frequency of 1 kHz, the real part of the relative dielectric constants ε_r of the alloys varies between -3.5×10^8 and -0.5×10^8 and increases with rising f, whereas the effects of T and σ on ε_r are opposite to those on ρ. Thermal property tests indicate that the thermal conductivities α of both alloys increase with T and eventually stabilize at 28.23 and 53.51 $W \cdot m^{-1} \cdot K^{-1}$, respectively, while the thermoelectric coefficients S are positively correlated with the heating rate, on the basis of comprehensive data analysis, multi-physical parameter (T, σ) dependent mathematical expressions for elastic modulus, strength, ρ, ε_r, α, and S were established, respectively. This work provides valuable insights into the material response mechanisms under complex service conditions, which are conducive to the optimization of alloy composition design and the promotion of their practical engineering applications.

Keywords: TiZrHf alloy; mechanical properties; electrical properties; thermal properties; electric–thermo–mechanical coupling

Check for updates

Academic Editor: Jiro Kitagawa

Received: 13 January 2026
Revised: 10 February 2026
Accepted: 12 February 2026
Published: 28 February 2026

Copyright: © 2026 by the authors. Licensee MDPI, Basel, Switzerland. This article is an open access article distributed under the terms and conditions of the Creative Commons Attribution (CC BY) license.

1. Introduction

The medium–high entropy alloys are a novel type of alloy composed of three or more equimolar metals. This type of alloy typically exhibits superior high-temperature resistance, fracture toughness, corrosion resistance, and oxidation resistance compared to traditional alloys. To date, numerous researchers have conducted extensive experimental measurements and theoretical investigations on the mechanical, electrical, and thermal parameters of medium–high entropy alloys.

It is generally accepted in the research community that the mechanical properties of medium–high entropy alloys are closely correlated with their phase structures, the types and proportions of constituent elements, and other relevant factors. For instance, Stepanov et al. [1] investigated the crystal structure, density, microhardness, and mechanical properties of the novel AlNbTiV high-entropy alloy. The results indicate that the alloy possesses a coarse-grained single body-centered cubic (BCC) phase structure, with a density of 5.59 $g \cdot cm^{-3}$ and a hardness ranging from 4315 to 4394 MPa. The compressive yield strength decreases from 1020 MPa at room temperature to 685 MPa at 800 °C and further to 158 MPa at 1000 °C; the specific yield strength of this alloy is comparable to that of multiphase refractory high-entropy alloys. Dong et al. [2] designed and synthesized an economical and efficient Co-free $AlCrFe_2Ni_2$ high-entropy alloy, based on the previously reported $AlCoCrFeNi_{2.1}$ eutectic high-entropy alloy. The tensile yield strength of $AlCrFe_2Ni_2$ alloy is 796 MPa, the ultimate tensile strength is 1437 MPa, and the elongation is 15.7%. These properties surpass those of most high-entropy alloys and are comparable to those of titanium-based superfine-grain alloys. In addition, the alloy consists of a planar face-centered cubic (FCC) phase, a disordered BCC (A2) phase, and an ordered BCC (B2) phase. The exceptional mechanical properties of the alloy are attributed to the spinodal decomposition of the BCC phase and the synergistic effect of the softer FCC phase combined with the harder BCC phase. Zhou et al. [3] designed and synthesized an isoatomic $Fe_{34}Cr_{34}Ni_{14}Al_{14}Co_4$ high-entropy alloy, which displayed a novel nanostructure consisting of multi-stage Fe-Cr-rich and Ni-Al-rich phases. This alloy demonstrates excellent compressive mechanical properties at both room temperature and high temperatures. Song et al. [4] prepared a medium entropy alloy $Fe_2NiCrNb_x$, which is composed of FCC and Laves phases. The results indicate that the addition of Nb promotes the formation of the primary Laves phase, and the hardness of the alloy increases with the concentration of Nb. The $Fe_2NiCrNb_{0.34}$ alloy demonstrates an excellent balance between strength and plasticity, achieving an ultimate tensile strength of 2267 MPa and a fracture strain of 30.8%. Wang et al. [5] summarized and explored the composition design, microstructural evolution, mechanical properties, and the mechanisms of strengthening and toughening in the CoCrFeNiNbx alloy system. Wei et al. [6] developed a novel BCC phase $AlCrFeMnNi_2$ high-entropy alloy with a distinctive sunflower-like eutectic microstructure. This alloy exhibits an impressive yield strength of 1206 MPa, a fracture strength of 3437 MPa, and a substantial compressive plastic strain of 37.5%. Zhang et al. [7] investigated the relationship between the fracture and failure behavior of $Ti_{48-x}Zr_xHf_{26}Nb_{26}$ (x = 14, 18, 22, 26, 30, 34) alloys and the contents of Ti and Zr. The results demonstrated that with the increase in Zr content, the failure mode of the alloys underwent a transition from intergranular fracture to transgranular fracture and then back to intergranular fracture. Furthermore, the alloys with high Ti content possessed superior toughness compared to those with high Zr content, where the elongation of the alloy with a Ti content of 34 at.% reached 17.83%, while that of the alloy with a Zr content of 34 at.% was 16.05%. Qi et al. [8] fabricated $Nb_{16}Si_xTi_yZr_zHf$ (x = 18, 22; y = 0, 4; z = 0, 4; at.%) alloys via the arc melting process, and systematically investigated the effects of Ti, Zr, and Hf elements on the phase composition, microstructure, fracture toughness, and crack propagation behavior of the alloys. The results indicated that the simultaneous addition of Ti, Zr, and Hf facilitated the eutectoid transformation of the $(Nb, X)_3Si$ phase to the $(Nb_{ss})/\gamma$-$(Nb, X)_5Si_3$ eutectic. The fine and lamellar microstructures of the $(Nb_{ss})/\gamma$-$(Nb, X)_5Si_3$ eutectic could induce crack bridging and branching, thereby effectively hindering crack propagation. The room-temperature fracture toughness of the $Nb_{16}Si_{22}Ti_4Zr_4Hf$ alloy was 11.62 $MPa \cdot m^{1/2}$, which was 87.7% higher than that of the $Nb_{16}Si_{18}Ti$ alloy.

In addition, some researchers have focused on the electrical properties of the alloy. For instance, Kannan et al. [9] investigated the dielectric constant (both real and imaginary parts), dielectric loss factor, and AC resistivity of $Ni_{0.5}Zn_{0.5}Fe_2O_4$ nano-ferrite particles at temperatures ranging from 700 to 1200 °C and frequencies from 0.1 Hz to 15 MHz. The results indicate that the dielectric constant decreases with increasing temperature, while the AC resistivity is approximately 10^7 Ω·m at room temperature. Sharma et al. [10] investigated the dielectric properties (temperature 300~380 K) of a quaternary ammonium salt glass alloy, specifically $(Se_{80}Te_{20})_{94-x}Ge_6Pb_x$ (x = 0, 2, 4, and 6). The results indicate that the dielectric constant, dielectric loss, and AC conductivity exhibit dependence on both temperature and frequency. Furthermore, the AC conductivity follows a power law distribution. Kerli et al. [11] employed the four-point method to investigate the resistivity of $Al_{85}Y_9Ni_6$ metallic glass within the temperature range of 300~877 K. The results indicate a significant decrease in resistivity between 527 and 632 K, which aligns with the findings from differential scanning calorimetry (DSC). Dagdelen et al. [12] prepared the shape memory alloy (SMA) $Ni_{50-x}Mn_{39}Sn_{11}Ta_x$ (x = 0, 1, 3) through arc melting under controlled atmospheric conditions. The results indicate that the SMA possesses high-temperature shape memory characteristics, and the phase transition temperature decreases with the addition of Ta. Furthermore, the alloy demonstrates higher resistivity in the martensitic phase compared to the austenitic phase. Ansari et al. [13] investigated the structural and electrical properties of the glass alloy $Se_{96-x}Sn_4Sb_x$ (x = 0, 2, 4, 6, 8). The results indicate that the binary specimen (x = 0) is polycrystalline, while the ternary specimens (x = 2, 4, 6, and 8) are amorphous. The dielectric constant and dielectric loss are highest in the binary specimen, whereas the ternary specimens exhibit lower values. The addition of Sb significantly reduced the conductivity by several orders of magnitude, transitioning the conduction mechanism from the CBH (Correlated Barrier Hopping) of NVAP (Non-Variable Amplitude Pulses) to the CBH conduction of IVPA (Inhomogeneous Variable Amplitude Pulses). Furthermore, some studies have indicated that medium–high entropy alloys exhibit unique electromechanical conversion characteristics. For instance, TiZrHf MEA exhibits a distinct electropolarization effect under impact loading [14]. Yang et al. [15] developed a theoretical model of current density-dependent yield strength for metallic materials based on the principle of thermo-mechanical equivalent energy density, with full consideration of the current-induced thermal and athermal effects. This model quantitatively describes the functional relationships between yield strength and elastic modulus, steady-state temperature, current density, thermal conductivity, and electrical resistivity under the action of an electric current.

Recently, researchers have shown significant interest in the thermal properties of alloys. Ying et al. [16] measured the thermal conductivity of Mg-Zn alloys at 293~523 K (Zn 0.5~5.0 wt%) using the laser flash method. The results indicate that the thermal conductivity of Mg-Zn alloys decreases with increasing Zn content. Pan et al. [17] investigated the effects of Sn content (3 wt%, 6 wt%, and 10 wt%) on the thermal conductivity of as-cast, homogeneous, and aged Mg-Sn alloys. The results indicate that the thermal conductivity of both as-cast and homogeneous Mg-Sn alloys decreases with increasing Sn content; the thermal conductivity of the as-cast alloy is higher than that of the homogeneous alloy. The thermal conductivity, electrical conductivity, melting enthalpy, specific heat capacity, and thermal diffusivity of as-cast A707 alloy were measured by Cadrl et al. [18] using the comparative cutting rod method. The results indicate that the thermal conductivity of as-cast A707 alloy decreases as the temperature increases. Ivanov et al. [19] investigated the low-temperature electrical and thermal conductivity of CoSi and $Co_{1-x}M_xSi$ alloys (where M = Fe, Ni, and $x \leq 0.06$). The results indicate that, compared to pure CoSi, the low-temperature electrical conductivity of $Co_{0.99}Fe_{0.01}Si$ alloy decreases by an order of magnitude. Below 20 K, the thermal conductivity of alloys containing either Fe or Ni

is several times larger than that of pure CoSi. Chen et al. [20] investigated the thermal characteristics of the Mg_xZn_xCu alloy (x = 1, 3, 5, 10 wt%). The results indicate that thermal conductivity gradually decreases with increasing Mg and Zn content. Notably, when x = 10 wt%, the thermal conductivity of the alloy remains as high as 136.5 W/(m·K).

Although there have been studies focusing on the mechanical, electrical, and thermal properties of medium–high entropy alloys separately, research on the multi-field coupling behavior is still relatively scarce. Especially, systematic experimental data and models for the alloys under mechanical–thermal–electric coupling conditions are still lacking. This paper aims to conduct a systematic study on the force-heat-electric coupling characteristics of TiZrHf and $TiZrHfCu_{0.8}$ alloys through an independently built multi-field coupling experimental platform, and establish the functional relationships of relevant physical parameters, in order to provide a theoretical and experimental basis for the application of this material in extreme environments.

2. Materials and Methods

2.1. Experimental Materials

TiZrHf and $TiZrHfCu_{0.8}$ cylindrical specimens (diameter Φ = 6 mm, height H = 15 mm) were selected for the experiment (Beijing Yanbang New Material Technology Co., Ltd., Beijing, China, purity ≥ 99.9%). The alloys were fabricated via vacuum arc melting, naturally cooled to room temperature, and subsequently processed by wire electrical discharge machining (WEDM) to obtain specimens with fixed geometric dimensions. Figure 1 and Table 1 present the XRD analysis results and typical phase analysis results of the original specimens, respectively.

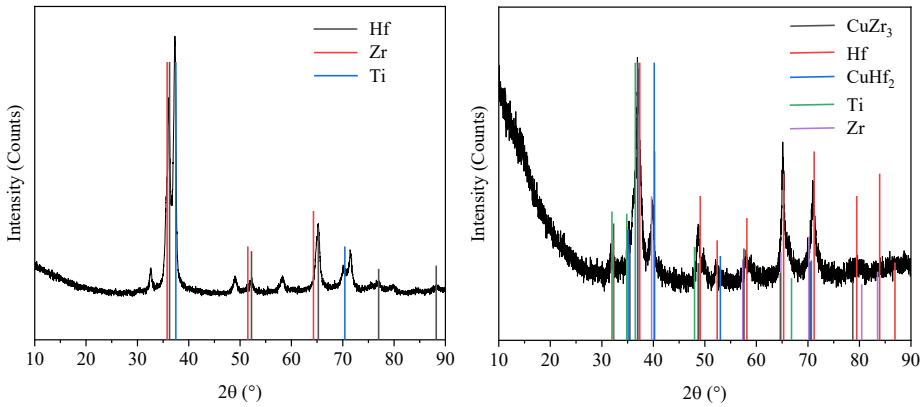


Figure 1. XRD analysis results and typical phase analysis results of the original specimens: (**a**) TiZrHf; (**b**) $TiZrHfCu_{0.8}$.

Table 1. Typical phase analysis results of the original specimens.

Materials	Chemical Formula	D	PDF-# [1]	#d/I [2]	Space Group	a [3]	b [3]	c [3]	Z
TiZrHf	Hf	C	89-5154	5	Im-3m (299)	3.500	3.500	3.500	2
TiZrHf	Zr	C	34-0657	10	Im-3m (229)	3.545	3.545	3.545	2
TiZrHf	Ti	C	44-1288	9	Im-3m (229)	3.306	3.306	3.306	2
$TiZrHfCu_{0.8}$	$CuZr_3$	C	65-2803	28	P4/mmm (123)	4.541	4.541	3.719	1
$TiZrHfCu_{0.8}$	Hf	C	70-2820	12	P63/mmc (194)	3.198	3.198	5.061	2
$TiZrHfCu_{0.8}$	$CuHf_2$	X	18-0440	35	I4/mmm (139)	3.170	3.170	11.133	2
$TiZrHfCu_{0.8}$	Ti	D	44-1294	17	P63/mmc (194)	2.951	2.951	4.683	2
$TiZrHfCu_{0.8}$	Zr	D	05-0665	25	P63/mmc (194)	3.232	3.232	5.147	2

[1] Powder Diffraction File number; [2] Relative intensity; [3] Lattice parameters along three directions.

The results verify the formation of a single BCC phase in TiZrHf, whereas $TiZrHfCu_{0.8}$ is composed of a dominant BCC phase with a minor Cu-rich FCC phase.

2.2. Experimental System

With cylindrical TiZrHf and $TiZrHfCu_{0.8}$ specimens as the research subjects, the mechanical, electrical, and thermal properties were measured through high temperature quasi-static compression experiments, electrical parameter measurement experiments under high temperature compression, and thermoelectric experiments. Figure 2 presents the schematic diagram of the experimental system.

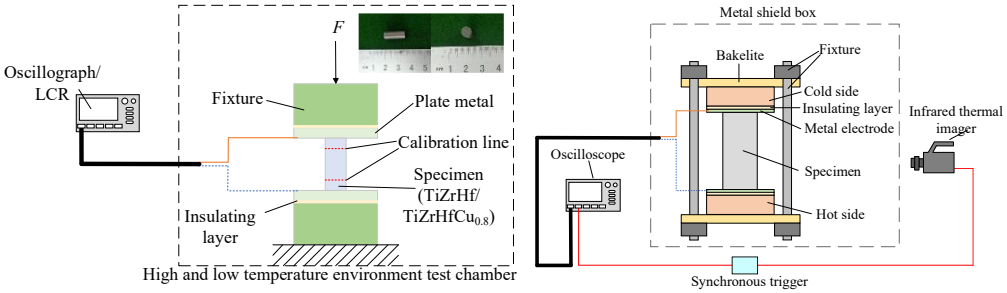


Figure 2. Experimental systems: (**a**) High temperature quasi-static compression and electrical parameter measurement; (**b**) Thermoelectricity measurement.

2.2.1. High Temperature Quasi-Static Compression

In the experiment, the mechanical properties of specimens at different temperatures were evaluated using a high temperature quasi-static compression testing system, including a universal testing machine with high temperature and low temperature environmental test chamber (WDW-100GD, Changchun New Testing Machine Co., Ltd., Changchun, China), fixtures, insulation layers, metal plates, and an oscilloscope (TEKTRONIX DPO3034, Tektronix Technology (China) Co., Ltd., Shanghai, China). One end of the fixture was fixed and connected to the universal testing machine, while the other end was attached to a metal plate with 0.8 cm × 12 cm × 12 cm (insulated with polyimide, PI). Meanwhile, the oscilloscope was positioned outside the high and low temperature environmental test chamber and connected to the upper and lower metal plates via coaxial cables to capture the electrical signals generated during the specimen's compression process.

To obtain accurate strain time histories of the specimens during the quasi-static compression process, two calibration lines were marked on the surface of the specimen, spaced 10 mm apart. The real time distance between the calibration lines was recorded using a camera. Before the experiment, the specimen was positioned at the center of the metal plate, and the temperature was adjusted. Once the target temperatures (T = 25 °C, 50 °C, 75 °C, and 100 °C) were reached, the temperature was maintained for 5 min. Then, the specimens were compressed at a speed of 1 mm/min. In this paper, each test condition was repeated on three independent samples. The data presented are the average values. Table 2 presents the experimental parameters for quasi-static compression at different temperatures.

Table 2. Experimental parameters for quasi-static compression.

No.	Specimens	T/°C	No.	Specimens	T/°C
1	TiZrHf	25	5	$TiZrHfCu_{0.8}$	25
2	TiZrHf	50	6	$TiZrHfCu_{0.8}$	50
3	TiZrHf	75	7	$TiZrHfCu_{0.8}$	75
4	TiZrHf	100	8	$TiZrHfCu_{0.8}$	100

2.2.2. Electrical Parameter Measurement

The experiment for measuring electrical parameters under high-temperature compression conditions was based on a high-temperature quasi-static compression experimental system. The electrical parameters (capacitance *C* and resistance *R*) of the specimens were tested using an LCR meter, as illustrated in Figure 2a. In the experiment, the specimens were subjected to pressures of 0 MPa, 300 MPa, 600 MPa, and 900 MP using the "force holding" mode. Then, T = 25 °C, 50 °C, 75 °C, and 100 °C were adjusted at each stress level to obtain the *C* and *R*. Table 3 shows the experimental parameters of electrical parameter measurement under high-temperature compression.

Table 3. Experimental parameters of electrical parameter measurement under high-temperature compression.

No.	Specimens	Stress/MPa	*T*/°C
9	TiZrHf	0, 300, 600, 900	25, 50, 75, 100
10	$TiZrHfCu_{0.8}$	0, 300, 600, 900	25, 50, 75, 100

2.2.3. Thermoelectric Experimental System

A thermoelectric experimental system was used to measure the temperature field characteristics and induced electrical output changes from specimens, as shown in Figure 2b. The thermoelectric experimental system consists of a fixed device, bakelite, a cold end with ice-water mixture, a hot end with heating table (HP-1010, Wenzhou Hanbang Electronics Co., Ltd., Wenzhou, China), an oscilloscope, and an infrared thermal imager (FLIR SC7000, FLIR Systems, Inc., Wilsonville, OR, USA). Before the experiment, bakelite (top)-cold end-insulation layer (PI)-electrode-specimen-electrode-insulation layer (PI)-hot end-bakelite were fixed by the fixed device. All the devices were placed in metal shielding boxes to shield them from external electromagnetic wave interference. The metal shielding box has a rectangular window at the position of the specimen, which is convenient for the infrared thermal imager to collect the temperature of the specimen. Both ends of the electrode of the specimen are connected to the oscilloscope and synchronously triggered with the infrared thermal imager.

After the experiment started, the temperature of the heating table was adjusted so that the temperature reached T_h = 50 °C, 100 °C, or 150 °C, and the oscilloscope and the infrared thermal imager were synchronously triggered to collect the voltage and temperature data (the data acquisition time was 400 s). Table 4 shows the experimental parameters of the thermoelectric experiment.

Table 4. Experimental parameters of the thermoelectric experiment.

No.	Specimens	T_h/°C	No.	Specimens	T_h/°C
11	TiZrHf	50	14	$TiZrHfCu_{0.8}$	50
12	TiZrHf	100	15	$TiZrHfCu_{0.8}$	100
13	TiZrHf	150	16	$TiZrHfCu_{0.8}$	150

3. Results

3.1. Mechanical Properties

The stress σ can be expressed as:

$$\sigma = \frac{F}{S_s} \quad (1)$$

where F is the pressure, S_s is the cross-section of the specimen. The strain ε of the specimen is calculated based on the distance of the calibration lines on the specimen (captured by the camera) during the experiment. The expression is as follows:

$$\varepsilon = \frac{\Delta L}{L} \tag{2}$$

where ΔL is the change in calibration line distance, and L is the initial distance between calibration lines. The quasi-static compressive σ-ε results of the specimens are presented in Figure 3.

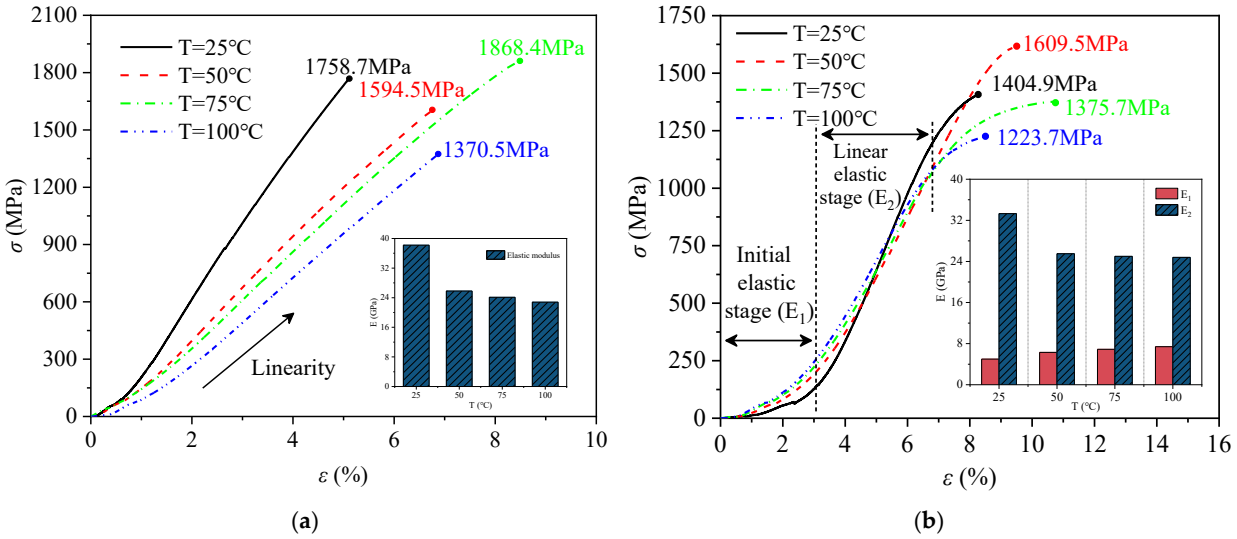


Figure 3. σ-ε curves of specimens at different T: (**a**) TiZrHf; (**b**) $TiZrHfCu_{0.8}$.

As shown in Figure 3a, the σ-ε relationship of TiZrHf is linear, and the elastic modulus E_{TZH} remains approximately constant. When the stress reaches the compressive strength, brittle failure of TiZrHf occurs. A comparison of the experimental results at various temperatures reveals that the E_{TZH} decreases with increasing T.

Compared to TiZrHf, the toughness of $TiZrHfCu_{0.8}$ is significantly enhanced due to the addition of Cu. During the quasi-static compression process, the $TiZrHfCu_{0.8}$ exhibits a multilinear response, undergoing an initial elastic stage, a linear elastic stage, a plastic deformation stage, and a failure stage. The viscous buffering effect of Cu in $TiZrHfCu_{0.8}$ results in a lower initial density compared to TiZrHf, allowing the initial elastic stage. At this stage, the elastic modulus of $TiZrHfCu_{0.8}$ increases with increasing T. When the strain of $TiZrHfCu_{0.8}$ reaches approximately 3%, the specimen becomes compacted and transitions into the linear elastic stage. At this stage, the elastic modulus is largest, while it gradually decreases with T. Subsequently, the specimen enters the plastic deformation stage, during which the elastic modulus gradually declines and approaches 0. Finally, the specimen fails when the local stress exceeds its maximum stress.

3.2. Compressive Fracture-Induced Electrical Response Characteristics

Figure 4 shows compressive fracture of TiZrHf and $TiZrHfCu_{0.8}$ induced electrical signals under different T.

As illustrated in Figure 4, the electrical signals show randomness due to the structural complexity, various metallic elements, and microdefects. The experiment demonstrates that the amplitude of the electrical signal generated by the specimen typically ranges from −1~1 V, and the timing of the electrical signal generation is inconsistent with the failure time of the specimen.

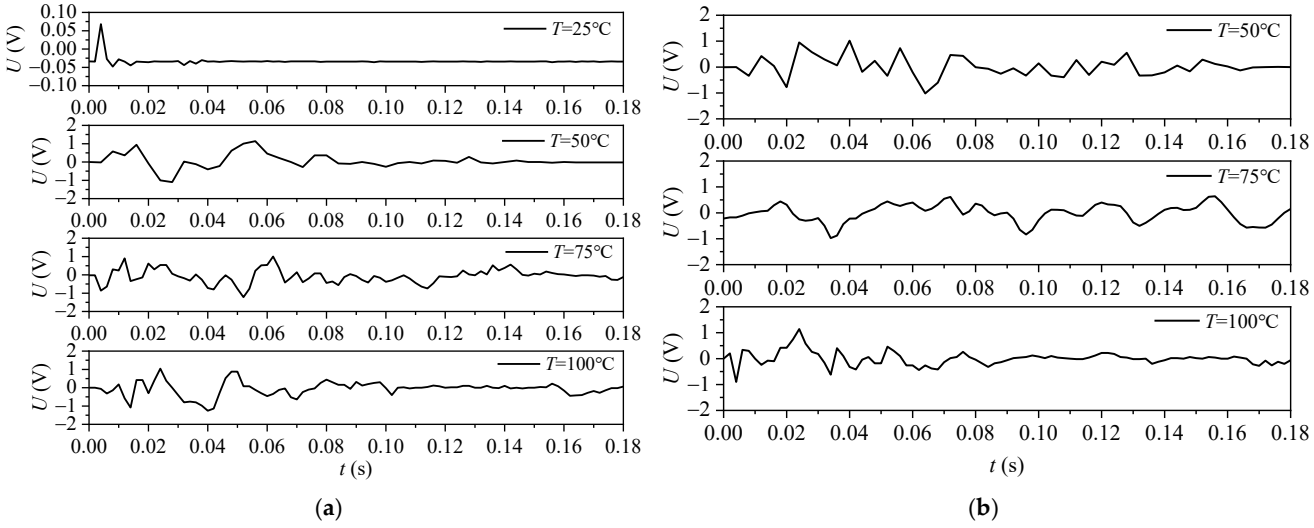


Figure 4. Compressive fracture-induced electrical signals under different T: (**a**) TiZrHf; (**b**) $TiZrHfCu_{0.8}$.

3.3. Electrical Properties

As shown in Figure 5, during the experiment, the LCR is connected with two square metal electrodes (the length is L, and the initial distance between the two electrodes is H). The LCR results can be regarded as the parallel results (parallel resistance and parallel capacitance) of the specimens and the related air domain. In order to accurately characterize the resistances and capacitances of the specimens, the LCR results are modified considering the influence of the air medium, as follows:

$$\frac{1}{R_{\mathrm{LCR}}} = \frac{1}{R} + \frac{1}{R_0} \tag{3}$$

where R_{LCR} is the resistance measured by LCR, R is the resistance of the specimen, and R_0 is the resistance of the air domain.

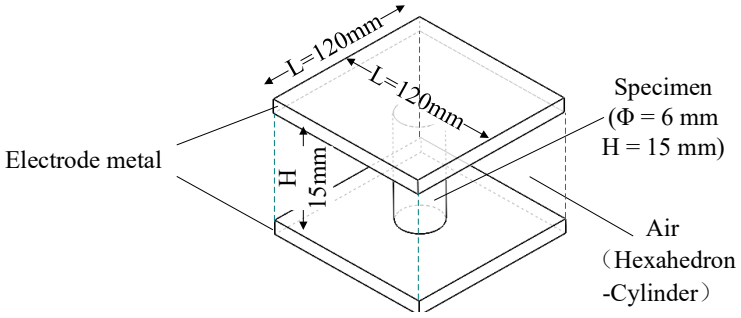


Figure 5. Schematic diagram of the specimen and air domain.

The relation between resistivity and resistance is:

$$R_0 = \frac{\rho_0 \cdot H(\sigma)}{S_{\mathrm{a}}} = \frac{\rho_0 \cdot H(\sigma)}{L^2 - S_s} \tag{4}$$

$$R = \frac{\rho \cdot H(\sigma)}{S_{\mathrm{s}}} \tag{5}$$

where ρ_0 and ρ are the resistivity of air and specimen, $H(\sigma)$ is the stress-related height of the specimen, and S_{a} and S_{s} are the cross-sectional areas of the air and specimen between the two electrodes. The modified resistivities of TiZrHf and $TiZrHfCu_{0.8}$ are shown in Figure 6.

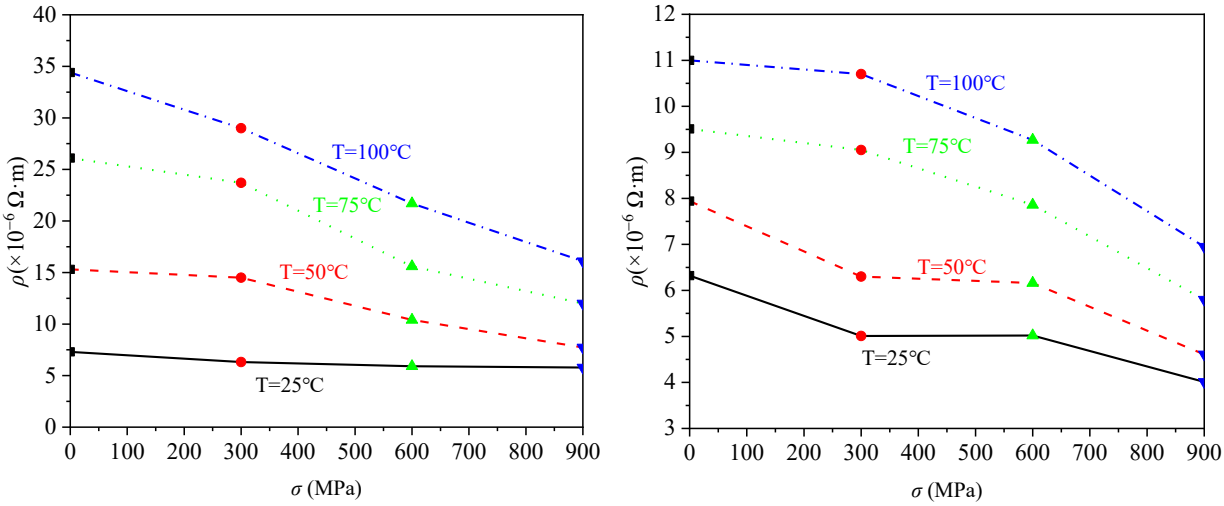


Figure 6. The modified resistivities of TiZrHf and $TiZrHfCu_{0.8}$: (**a**) TiZrHf; (**b**) $TiZrHfCu_{0.8}$.

As can be seen from Figure 6a, the resistivity of TiZrHf is 7.3×10^{-6} Ω·m at 0 MPa and 25 °C. In addition, the resistivity of TiZrHf increases with increasing T, e.g., the resistivity of TiZrHf reaches 34.4×10^{-6} Ω·m at 100 °C. Beyond that, the resistivity of TiZrHf decreases with increasing σ, e.g., the resistivity of TiZrHf is 5.78×10^{-6} Ω·m at 25 °C and σ = 900 MPa. The results in Figure 6b indicate that the effect of T and σ on the resistivity of $TiZrHfCu_{0.8}$ is similar to that of TiZrHf. Moreover, because $TiZrHfCu_{0.8}$ contains Cu components, Cu increases the conductivity of $TiZrHfCu_{0.8}$. The resistivity of $TiZrHfCu_{0.8}$ is lower than that of TiZrHf under the same conditions due to the addition of Cu (the conductivity of Cu is larger).

The equation for parallel capacitance can be expressed as:

$$C_{LCR} = C_0 + C \tag{6}$$

where C_{LCR} is the capacitance measured by LCR, C is the capacitance of the specimen, and C_0 is the capacitance of the air domain. The relationship between the real part of the relative dielectric constant ε_r and capacitance C is:

$$C_0 = \frac{\varepsilon_0 \cdot S_a}{H(\sigma)} \tag{7}$$

$$C = \frac{\varepsilon_0 \cdot \varepsilon_r \cdot S_s}{H(\sigma)} \tag{8}$$

where, ε_0 is the vacuum dielectric constant. Figures 7 and 8 show the ε_r of TiZrHf and $TiZrHfCu_{0.8}$, respectively.

As shown in Figure 8, the ε_r of TiZrHf are all negative and increase with increasing frequency f, showing a nonlinear relationship. For example, under the conditions of 0 MPa and 25 °C, the ε_r of TiZrHf at 1 kHz is -1.87×10^8. When f reaches 200 kHz, the slopes of the εr-f curve are almost zero; meanwhile, ε_r reaches its maximum of -0.13×10^8. Under the same pressure, the ε_r of TiZrHf decreases as the temperature rises. At the same T, the ε_r of TiZrHf increases with increasing σ, and the increase effect is independent of f. By comparing Figure 8 with Figure 7, it can be seen that the effect of f, σ, and T on the ε_r of $TiZrHfCu_{0.8}$ is similar to that of TiZrHf. Under the same conditions, the ε_r of $TiZrHfCu_{0.8}$ is larger than that of TiZrHf.

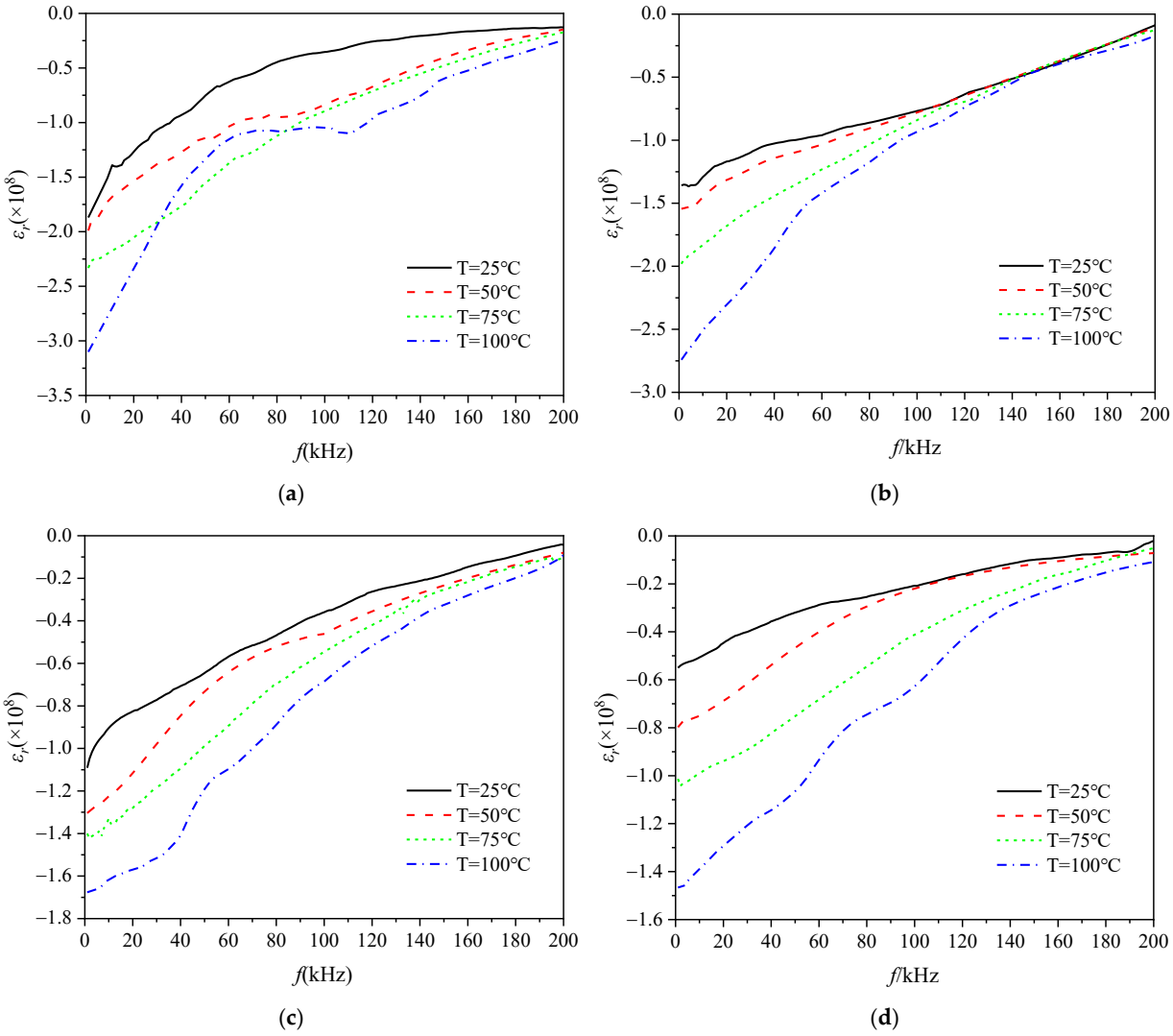


Figure 7. ε_r of TiZrHf under different T and σ: (**a**) 0 MPa; (**b**) 300 MPa; (**c**) 600 MPa; (**d**) 900 MPa.

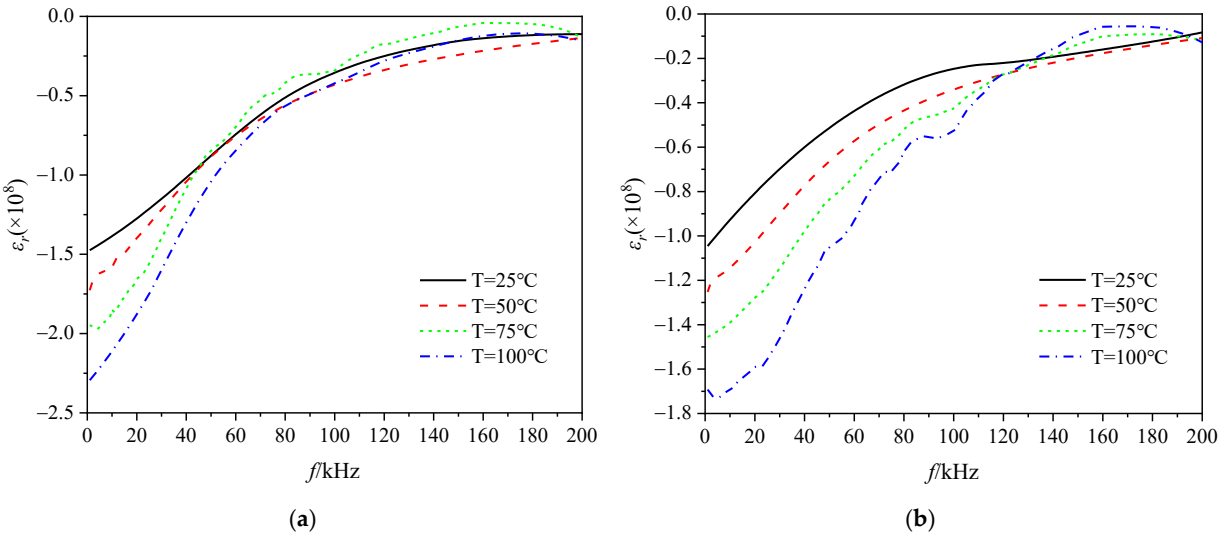


Figure 8. *Cont.*

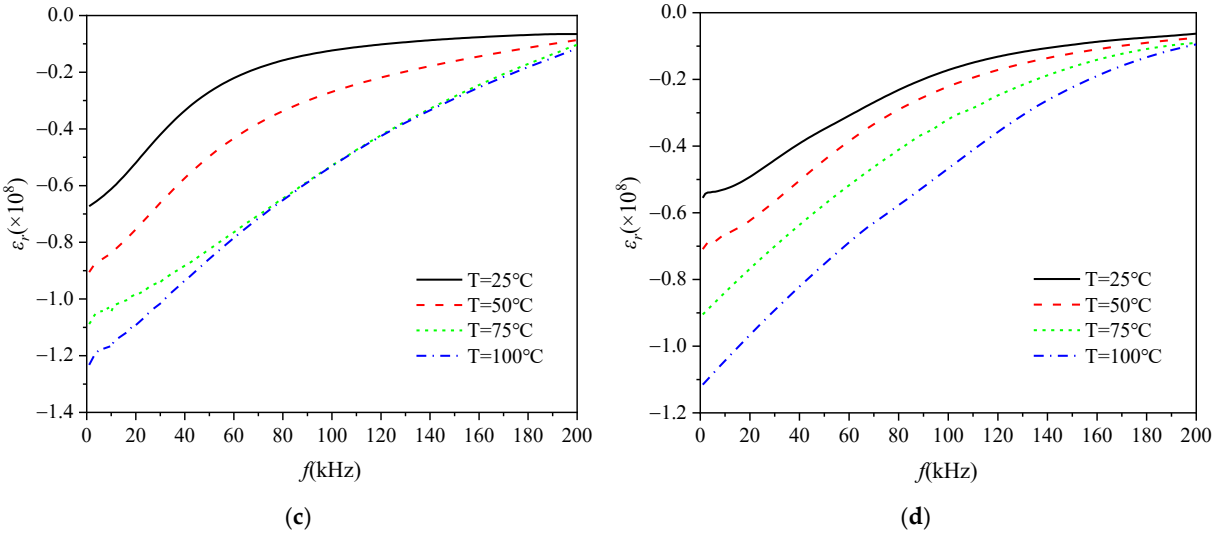


Figure 8. ε_r of $TiZrHfCu_{0.8}$ under different T and σ: (**a**) 0 MPa; (**b**) 300 MPa; (**c**) 600 MPa; (**d**) 900 MPa.

3.4. Thermal Property

Based on data collected by the infrared thermal imager, the temperature field distribution characteristics of TiZrHf and $TiZrHfCu_{0.8}$ at T_h = 50 °C, 100 °C, and 150 °C are analyzed. Taking T_h = 100 °C as an example, the results are shown in Figure 9.

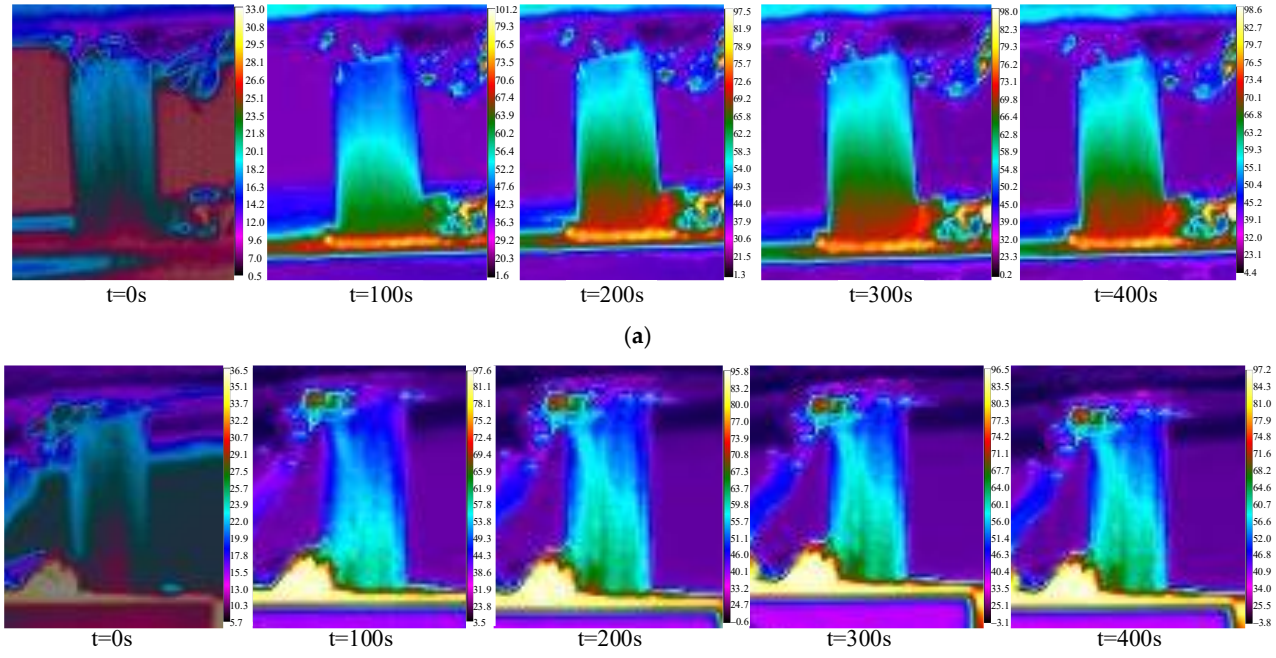


Figure 9. The temperature field distribution of TiZrHf and $TiZrHfCu_{0.8}$ (T_h = 100 °C): (**a**) TiZrHf; (**b**) $TiZrHfCu_{0.8}$.

To further analyze the distribution law of T, points P1~P5 are uniformly selected along the z-axis, as shown in Figure 10. Then, the average temperature $\overline{T}$ of TiZrHf and $TiZrHfCu_{0.8}$ are obtained by calculating the T of all points at the same height z, as shown in Figures 11 and 12.

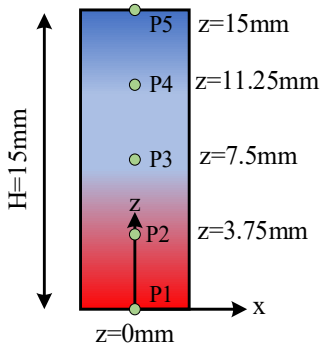


Figure 10. Schematic diagram of point selection.

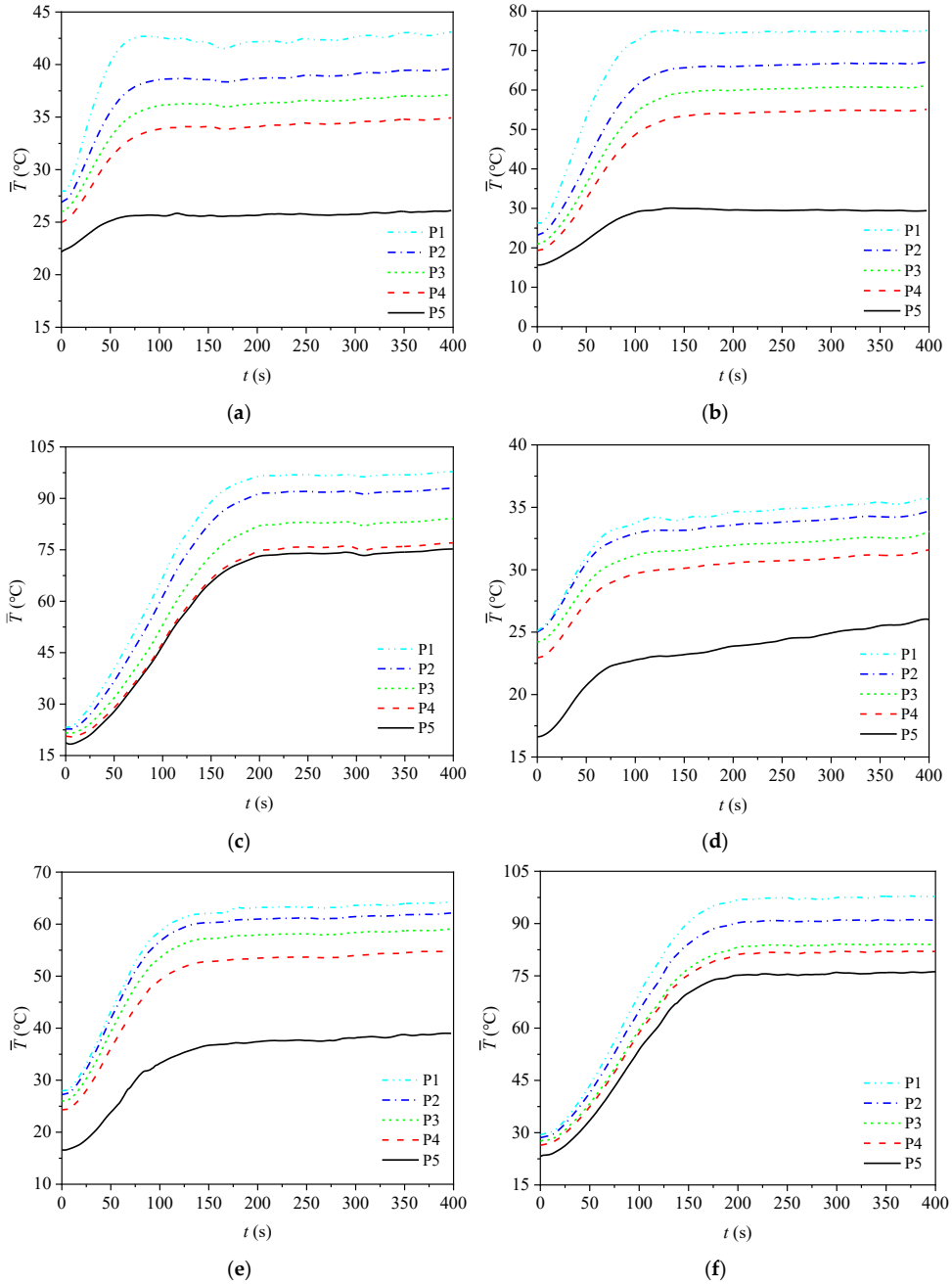


Figure 11. The $\overline{T}$ time history of TiZrHf and $TiZrHfCu_{0.8}$: (**a**) TiZrHf, 50; (**b**) TiZrHf, 100 °C; (**c**) TiZrHf, 150 °C; (**d**) $TiZrHfCu_{0.8}$, 50; (**e**) $TiZrHfCu_{0.8}$, 100 °C; (**f**) $TiZrHfCu_{0.8}$, 150 °C.

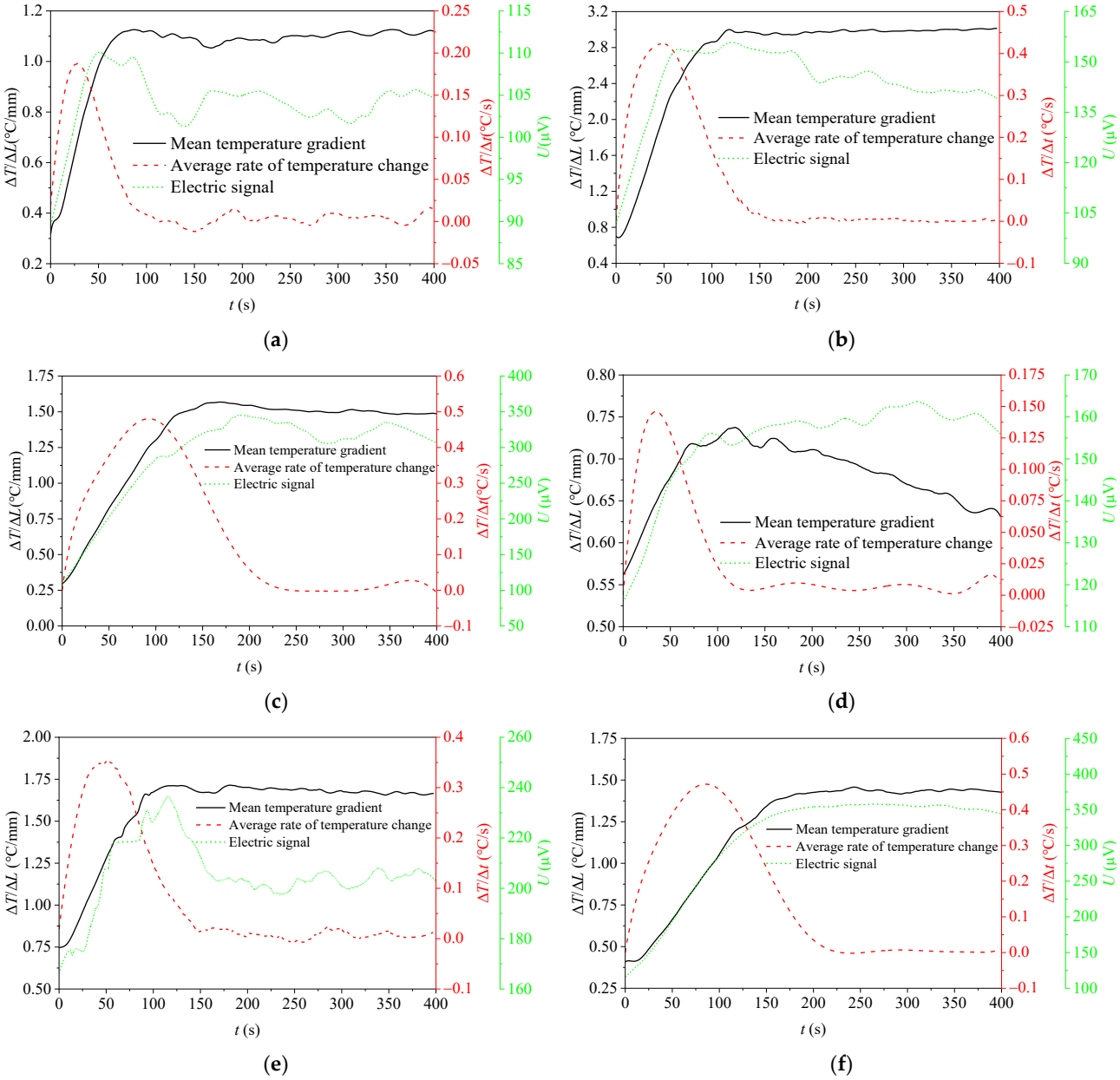


Figure 12. The relationship between U and T of TiZrHf and $TiZrHfCu_{0.8}$: (**a**) TiZrHf, 50 °C; (**b**) TiZrHf, 100 °C; (**c**) TiZrHf, 150 °C; (**d**) $TiZrHfCu_{0.8}$, 50 °C; (**e**) $TiZrHfCu_{0.8}$, 100 °C; (**f**) $TiZrHfCu_{0.8}$, 150 °C.

As shown in Figure 11, under T_h = 50 °C, the $\overline{T}$ at each point P1~P5 on TiZrHf gradually increase with increasing t until it reaches the stable values ($t \approx 60$ s). The comparison in Figure 11a indicates that $\overline{T}$ of P1 is the largest due to the effect of the hot end, showing a stable temperature T_s *of* about 43 °C; while $\overline{T}$ of P5 is the smallest due to the effect of the cold end, the T_s is approximately 26 °C. Beyond that, the temperature difference $\Delta\overline{T}$ between P4 and P5 (about 8 °C) is much larger than that between P1, P2, P3, and P4 (about 2 °C). This phenomenon may occur because P5 is situated closest to the cold end, which absorbs heat at a faster rate. However, the heat transfer rate of TiZrHf is limited due to its low thermal conductivity. Consequently, the heat transferred from P4 to P5 is absorbed by the cold end before it can accumulate, allowing P5 to quickly achieve a balance between heat intake and exhaust.

As shown in Figure 11c, the $\overline{T}$ curves at each point of TiZrHf exhibited slight variations under T_h = 150 °C. Due to the larger T_h, the time required for the stable T of P1~P5 is extended, approximately 180 s. Compared with Figure 11a, the T_s of P1~P5 are larger,

e.g., the T_s of P1 is approximately 97 °C, while the T_s of P5 is around 74 °C. In contrast to Figure 11a, once the stable temperature was achieved, the temperature difference between P1 and P5 is close, without a significant temperature disparity between P4 and P5. This phenomenon may be attributed to the increasing T_h, which significantly enhances the thermal conductivity of TiZrHf, making it substantially greater than that between the specimen and the cold end. As a result, the specimen accumulates heat at P5, leading to an increase in temperature.

As shown in Figure 11d–f, the $\overline{T}$ curves at P1~P5 of $TiZrHfCu_{0.8}$ are similar to TiZrHf. However, under the same T_h, the T_s at each point of $TiZrHfCu_{0.8}$ are consistently lower than those of TiZrHf. This discrepancy may be attributed to the increased copper content in $TiZrHfCu_{0.8}$, which enhances the thermal conductivity between the material and the cold end, consequently resulting in a reduction in T_s.

3.5. Thermoelectric Properties

The temperature gradient was calculated from the temperature difference and the distance between adjacent points. Taking P1 and P2 as an example, the temperatures at these two points were measured by the infrared thermal imager; the temperature gradient was then obtained by dividing their temperature difference by the distance between P1 and P2.

The matching relationship between the thermoelectric voltage U collected by the oscilloscope and the temperature characteristics (temperature gradient $\Delta T/\Delta L$ and heating rate $\Delta T/\Delta t$) is shown in Figure 12.

It can be observed from Figure 12 that, under different T_h, both the average $\Delta T/\Delta L$ and U of the specimen exhibit a trend of initially increasing followed by stabilization. Furthermore, the times required for the stable $\Delta T/\Delta L$ and U are approximately the same. In addition, the variation pattern of the average heating rate $\Delta T/\Delta t$ of the specimen is as follows: rising from 0 °C/s to the maximum value, and decreasing back to 0 °C/s, then stabilizing.

Under T_h = 50 °C, the TiZrHf achieved a stable state at 75 s; meanwhile, the average $\Delta T/\Delta L$ at the stable state is about 1.1 °C/mm, and the average U measured is approximately 105 μV. Differently, the average maximum $\Delta T/\Delta t$ is about 0.18 °C/s at 25 s; however, the stable state begins at about 100 s. Under T_h = 100 °C and 150 °C, the average $\Delta T/\Delta L$ of TiZrHf and the U at the stable state are larger than that under T_h = 50 °C.

As for $TiZrHfCu_{0.8}$, the smaller $\Delta T/\Delta L$ and $\Delta T/\Delta t$ can be observed compared with TiZrHf under the same T_h. Nonetheless, the U of $TiZrHfCu_{0.8}$ is larger than TiZrHf.

4. Discussion

4.1. Effect of T on Mechanical Parameters

4.1.1. Quasi-Static Mechanical Properties of TiZrHf

(1) Elastic modulus

The stress–strain curves of TiZrHf are approximately linear. Therefore, a linear elastic constitutive model is adopted to characterize its stress–strain relationship, and the expression is as follows:

$$\sigma = E \cdot \varepsilon \tag{9}$$

The Johnson–Cook constitutive model is an ideal plastic strength model that can effectively reflect the strain hardening, strain rate strengthening effect, and temperature softening effect of metallic materials. The expression of the Johnson–Cook constitutive model is:

$$\sigma = \left(A + B\varepsilon_{\mathrm{p}}^{n}\right)\left(1 + C\ln\frac{\dot{\varepsilon}_{\mathrm{p}}}{\dot{\varepsilon}_{0}}\right)\left[1 - \left(\frac{T - T_{\mathrm{r}}}{T_{\mathrm{m}} - T_{\mathrm{r}}}\right)^{m}\right] \tag{10}$$

where A is the yield strength of materials under quasi-static conditions, B is the strain hardening constant, n is the strain hardening exponent, ε_{p} is the plastic strain, C is the strain rate strengthening constant, $\dot{\varepsilon}_{\mathrm{p}}$ is the plastic strain rate, $\dot{\varepsilon}_{0}$ is the reference strain rate, T_{m} is the melting temperature, T_{r} is the reference temperature, and m is temperature softening parameter.

In this paper, the effect of T on E can be characterized using the temperature term in the Johnson–Cook model. The fitting results are:

$$E = 38.2\left[1 - \left(\frac{T - 25}{7662.56}\right)^{0.197}\right] \tag{11}$$

(2) The compression strength

Based on the compression strength values $\sigma_{\max}$ of TiZrHf obtained from the quasi-static compression experiments under different T. Taking T as the independent variable, a linear fitting is conducted to obtain the compression strength-temperature relationship of TiZrHf, and the expression is as follows:

$$\sigma_{\max} = -5.08T + 1870.70 \tag{12}$$

4.1.2. Quasi-Static Mechanical Properties of $TiZrHfCu_{0.8}$

(1) Multilinear mechanical behavior

The stress–strain curve of $TiZrHfCu_{0.8}$ is approximately an inverted "S" shape, and it exhibits multilinear mechanical characteristics during the elastic stage. The Johnson–Cook constitutive model (or elastoplastic model) used to describe linear elasticity is no longer appropriate. Given the inherent multi-stage nature of hyperelastic models from a mathematical perspective, this work employs hyperelastic models (e.g., the Yeoh model) to characterize the multilinear mechanical behavior of $TiZrHfCu_{0.8}$, thereby achieving full representation of the overall stress–strain response with a single constitutive model. The related strain energy function can be expressed as:

$$W_{Yeoh} = C_{10}(I_1 - 3) + C_{20}(I_1 - 3)^2 + C_{30}(I_1 - 3)^3 \tag{13}$$

where I is the first invariant of the strain tensor, considering the effect of temperature, Equation (13) can be modified by adding *a* T term, as:

$$W_{\mathrm{Yeoh}} = \left[C_{10}(I_1 - 3) + C_{20}(I_1 - 3)^2 + C_{30}(I_1 - 3)^3\right]\left(1 - \frac{T - 25}{T_{\mathrm{n}} - T}\right) \tag{14}$$

Based on the experimental results, the following expression can be obtained:

$$W_{\mathrm{Yeoh}} = \left[-48(I_1 - 3) + 5390(I_1 - 3)^2 - 2.896 \times 10^5(I_1 - 3)^3\right]\left(1 - \frac{T - 25}{-18.72 - T}\right) \tag{15}$$

where T_{n} is the parameter.

(2) Quasi-plastic stage

In this paper, the Johnson–Cook constitutive model is adopted to describe the quasi-plastic stage of $TiZrHfCu_{0.8}$. Since the specimen is approximately in a state of mechanical

equilibrium during the quasi-static compression process, the effect of strain rate $\dot{\varepsilon}$ is not considered, and the Johnson–Cook constitutive model can be simplified as:

$$\sigma = \left(A + B\varepsilon_{\mathrm{p}}^{n}\right)\left[1 - \left(\frac{T - T_r}{T_m - T_r}\right)^{m}\right] \tag{16}$$

By fitting the experimental data, the plastic stress can be obtained.

$$\sigma = \left(1148.53 + 11590.75\varepsilon_p^{0.84}\right)\left[1 - \left(\frac{T - 25}{140.29}\right)^{1.928}\right] \tag{17}$$

(3) The yield limit

According to the yield limits of $TiZrHfCu_{0.8}$ under different T, taking T as the independent variable, polynomial fitting is carried out to obtain the expression of the yield limits of $TiZrHfCu_{0.8}$, as

$$\sigma_{\mathrm{s}} = 1117.87 + 2.68T - 0.06T^2 \tag{18}$$

4.1.3. Verification of Mechanical Parameters

In order to verify the accuracy of the mechanical parameters, the Abaqus software 2020 is used in combination with the corresponding constitutive model and parameters to conduct numerical simulations of the high-temperature quasi-static compression. The results are shown in Figure 13.

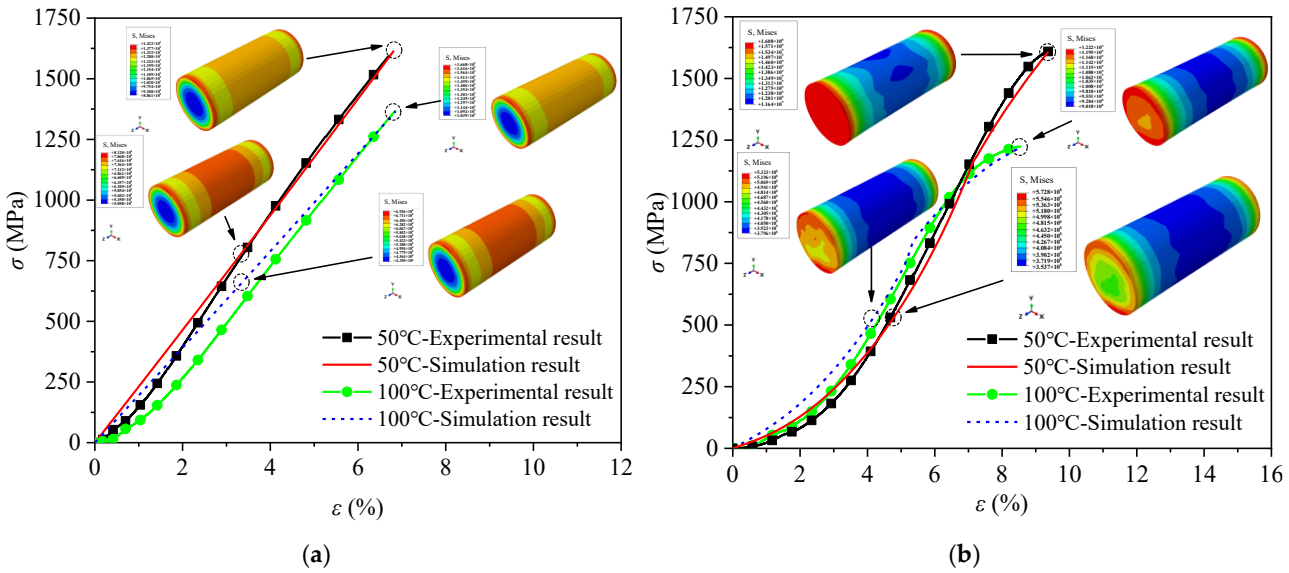


Figure 13. Comparison between the numerical simulation results and the experimental results: (**a**) TiZrHf; (**b**) $TiZrHfCu_{0.8}$.

As shown in Figure 13, taking the numerical simulation results under the conditions of 50 °C and 100 °C as examples, the numerical simulation results are in good agreement with the experimental results (the relative error is generally smaller than 5%, generally). In general, the proposed constitutive model indicates a negative correlation between elastic modulus, strength, and temperature, in agreement with the findings presented in Refs. [21,22].

4.2. Effect of Temperature/Stress on the Electrical Properties

4.2.1. Relative Dielectric Constant

There has been a lot of discussion about the ε_r of metals. Currently, in various calculations, the Drude equation based on the free electron gas model is mainly used to obtain the dielectric constant of metals, the expression is [23]:

$$\varepsilon(\omega) = \varepsilon_1(\omega) - j\varepsilon_2(\omega) \tag{19}$$

$$\varepsilon_1 = 1 - \frac{\omega_p^2}{1 + f^2\tau^2} \tag{20}$$

$$\varepsilon_2 = \frac{\omega_p^2 \cdot \tau}{\omega(1 + f^2\tau^2)} \tag{21}$$

where ω_p is the resonance frequency of metallic plasma, τ is the relaxation time of electrons, and ω is the frequency of the electromagnetic wave.

Only considering the real part of ε_r, parameter a is introduced to correct the Drude Formula (19), and the expression is:

$$\varepsilon_r = a - \frac{\omega_p^2}{1 + f^2\tau^2} \tag{22}$$

By fitting the experimental data of TiZrHf under the conditions of 25 °C and 0 MPa, the dielectric constant ε_r of TiZrHf material is determined as:

$$\varepsilon_r = -4.05 \times 10^6 - \frac{1.83 \times 10^8}{1 + 5.37 \times 10^{-10} f^2} \tag{23}$$

Considering the effect of stress, ε_r can be modified as:

$$\varepsilon_r = \left(a - \frac{\omega_p^2}{1 + f^2\tau^2}\right)(1 + b\sigma) \tag{24}$$

According to Barrett's law, the relationship between the initial ferroelectric expansion coefficient α_P and T is

$$\alpha_P(T) = \alpha_T^{(P)} \left[\frac{T_q^{(P)}}{2} \coth\left(\frac{T_q^{(P)}}{2T}\right) - T_c^{(P)}\right] \tag{25}$$

where $T_q^{(P)}$ is the quantum vibration temperature; $T_c^{(P)}$ is the "effective" Curie temperature. By combining Equations (24) and (25), the relationship between ε_r and temperature, stress can be derived as follows:

$$\varepsilon_r(T, \sigma) = \left(a - \frac{\omega_p^2}{1 + f^2\tau^2}\right)(1 + b\sigma)\alpha_P(T) \tag{26}$$

By substituting the experimental results and determining ε_r of TiZrHf and $TiZrHfCu_{0.8, it}$ can be obtained as:

$$\begin{cases} \text{TiZrHf}: \ \varepsilon_r(T,\sigma) = \left(-2.047 \times 10^7 - \frac{9.2740 \times 10^8}{1 + 5.366 \times 10^{-10} f^2}\right)\left(1 - 6.694 \times 10^{-4}\sigma\right)\left[\coth\left(\frac{140.7}{T}\right) - 0.8003\right] \\ \text{TiZrHfCu}_{0.8}: \varepsilon_r(T,\sigma) = \left(1.01 \times 10^6 - \frac{4.935 \times 10^7}{1 + 2.7168 \times 10^{-10} f^2}\right)\left(1 - 8.191 \times 10^{-4}\sigma\right)\left[\coth\left(\frac{38.09}{T}\right) + 1.9535\right] \end{cases} \tag{27}$$

Figure 14 shows the comparison between the fitting results and the experimental results.

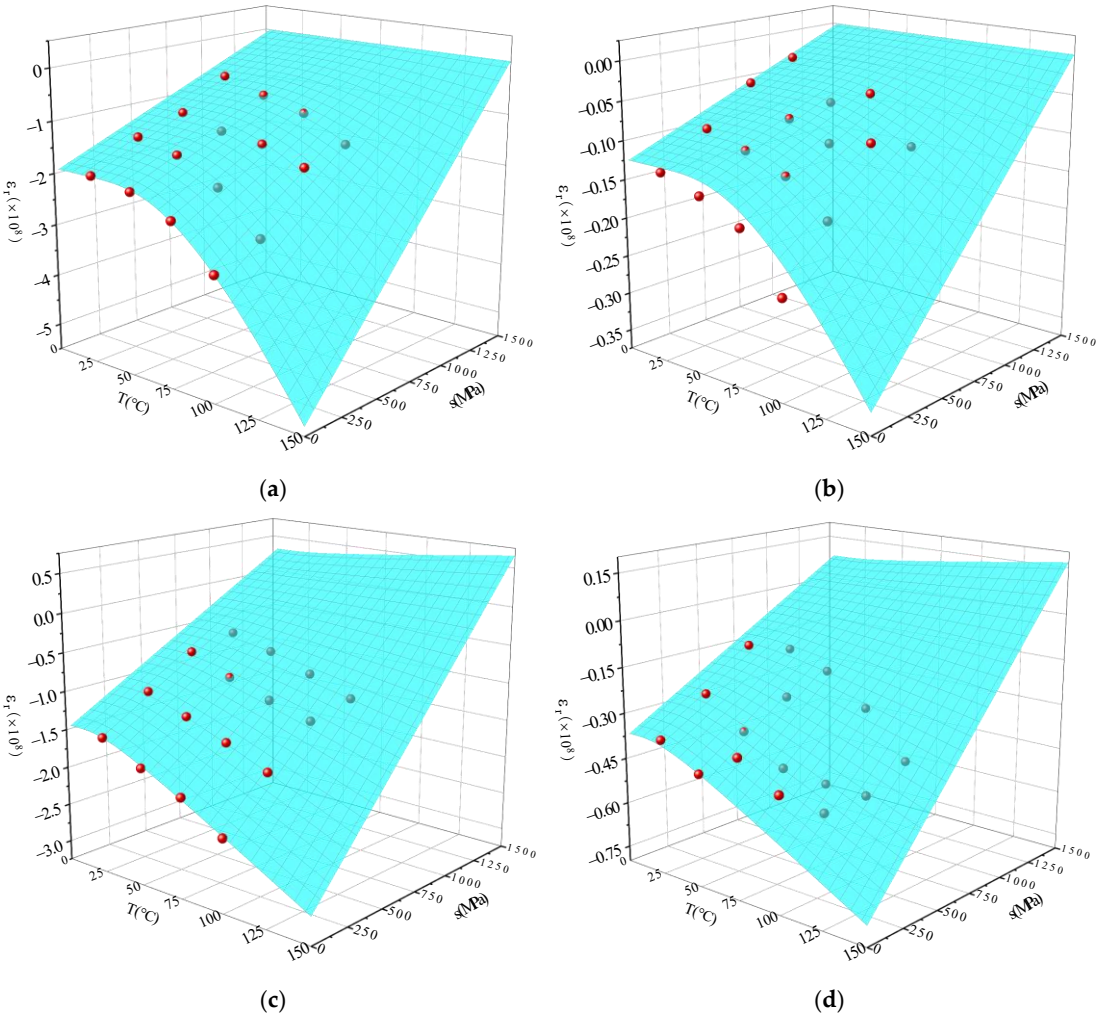


Figure 14. Comparison between the fitting results and the experimental results: (**a**) 1 kHz, TiZrHf; (**b**) 200 kHz, TiZrHf; (**c**) 1 kHz, $TiZrHfCu_{0.8}$; (**d**) 100 kHz, $TiZrHfCu_{0.8}$.

4.2.2. Resistivity

From the experimental results, it is known that the electrical resistivity ρ of both TiZrHf and $TiZrHfCu_{0.8}$ exhibits an approximate linear relationship with T and σ. Therefore, this paper proposes that ρ can be expressed as the product of a linear function of temperature and a linear function of stress, which is formulated as:

$$\rho(T,\sigma) = a + (b\sigma + c)(T + d) \tag{28}$$

By fitting the experimental data, the ρ of TiZrHf and $TiZrHfCu_{0.8}$ are determined as follows:

$$\begin{cases} \text{TiZrHf}: \ \rho(T,\sigma) = 3.811 \times 10^{-6} + \left(-2.606 \times 10^{-10}\sigma + 3.74 \times 10^{-7}\right)(T - 16.06) \\ TiZrHfCu_{0.8}: \ \rho(T,\sigma) = 3.482 \times 10^{-6} + \left(-5.257 \times 10^{-11}\sigma + 8.341 \times 10^{-8}\right)T \end{cases} \tag{29}$$

In Equation (29), the stress-dependent coefficient is negative, indicating that an increase in stress leads to a reduction in electrical resistivity. This conclusion is applicable to most medium–high entropy alloys [24,25].

4.3. Thermal Parameters

4.3.1. Thermal Conductivity

In this paper, the one-dimensional heat conduction equation is used to describe the heat flow inside the test piece, and the expression is:

$$\frac{\partial T(x,t)}{\partial t} = \kappa \frac{\partial^2 T(x,t)}{\partial x^2} \tag{30}$$

where $u(x, t)$ is the T distribution with time t and spatial coordination x, and κ is the thermal conductivity. The experimental results show that there is a correlation between the thermal conductivity and T, and the thermal conductivity of the material is determined by fitting.

$$\begin{cases} \text{TiZrHf}: \ \kappa = 28.23 - \frac{270.8}{T-14.55} \\ \text{TiZrHfCu}_{0.8}: \ \kappa = 53.51 - \frac{77.08}{T-16.67} \end{cases} \tag{31}$$

4.3.2. Thermoelectric Coefficient

In this paper, the Seebeck effect is used to characterize the voltage difference U caused by the temperature difference ΔT at both ends of the alloys. The calculation of the Seebeck coefficient S is as follows:

$$S = \frac{U}{\Delta T} \tag{32}$$

Considering the effect of the heating rate, S can be modified as

$$S = S_c + k\frac{\partial T}{\partial t} = \frac{U}{\Delta T} \tag{33}$$

where S_c is the constant, k is the heating rate-related parameter. Based on the experimental results, the modified S can be obtained as:

$$\begin{cases} \text{TiZrHf}: \ U = \left(6.877 \times 10^{-6} + 1.501 \times 10^{-6}\frac{\partial T}{\partial t}\right)\Delta T \\ \text{TiZrHfCu}_{0.8}: \ U = \left(1.509 \times 10^{-5} + 2.767 \times 10^{-6}\frac{\partial T}{\partial t}\right)\Delta T \end{cases} \tag{34}$$

The thermoelectric experimental results under the conditions of T_h = 50 °C and 100 °C are selected, and compared with the voltage time history calculated based on the modified S. The results are shown in Figure 15.

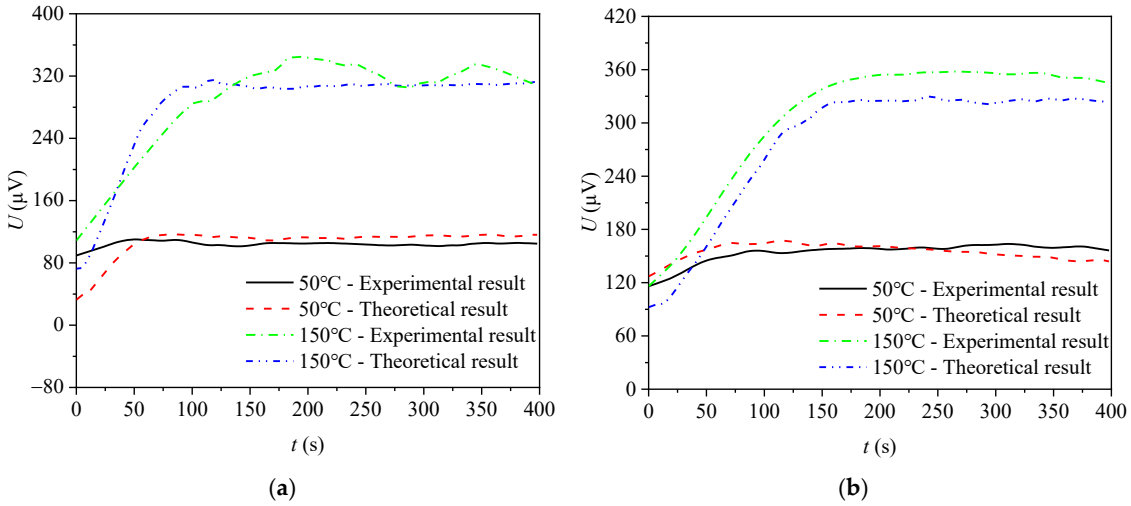


Figure 15. Comparison between the thermoelectric experimental results and the theoretical results: (**a**) TiZrHf; (**b**) $TiZrHfCu_{0.8}$.

As shown in Figure 15, the theoretical calculation results are in good agreement with the experimental voltage-time history. Among them, the average errors of TiZrHf and $TiZrHfCu_{0.8}$ under the condition of T_h = 50 °C are 3.85% and 0.65%, respectively; the average errors of the two under the condition of T_h = 150 °C are 2.41% and 9.39%, respectively. Overall, the modified Seebeck coefficient is applicable to the characterization of the thermoelectric properties of TiZrHf-based alloys.

5. Conclusions

In this paper, the electric–thermo–mechanical coupling characteristics of TiZrHf and $TiZrHfCu_{0.8}$ alloys have been investigated based on the self-developed experimental test system. Based on the analysis of experimental data and numerical simulations, multi-physical parameter (T, σ) expressions for elastic modulus, strength, ρ, ε_r, α, and S are obtained and verified. The conclusions are as follows:

The compressive mechanical properties of TiZrHf and $TiZrHfCu_{0.8}$ exhibit elastoplastic and superelastic-plastic mechanical behaviors, respectively, with both elastic modulus and ultimate strength decreasing with temperature T. The constitutive model can be expressed as:

$$\begin{cases} \text{TiZrHf}: \begin{cases} E = 38.2\left[1-\left(\frac{T-25}{7662.56}\right)^{0.197}\right] \\ \sigma_{max} = -5.08T + 1870.70 \end{cases} \\ \text{TiZrHfCu}_{0.8}: \begin{cases} W_{Yeoh} = \left[-48(I_1-3)+5390(I_1-3)^2-2.896\times10^5(I_1-3)^3\right]\times\left(1-\frac{T-25}{-18.72-T}\right) \\ \sigma = \left(1148.53+11590.75\varepsilon_p^{0.84}\right)\left[1-\left(\frac{T-25}{140.29}\right)^{1.928}\right] \\ \sigma_s = 1117.87+2.68T-0.06T^2 \end{cases} \end{cases} \quad (35)$$

Electrical property analysis shows that ρ of the two alloys ranges from 3 to 35×10^{-6} Ω·m ($TiZrHfCu_{0.8}$ has a lower value, independent of the test frequency f), increasing with T and decreasing with stress σ. Their real part of relative dielectric constants ε_r range from -3.5×10^8 to -0.5×10^8 (at 1 kHz) and increase with f; however, the effect of T and σ on ε_r are opposite to ρ. The electric parameters can be expressed as:

$$\begin{cases} \text{TiZrHf}: \begin{cases} \varepsilon_r(T,\sigma) = \left(-2.047\times10^7-\frac{9.2740\times10^8}{1+5.366\times10^{-10}f^2}\right)\left(1-6.694\times10^{-4}\sigma\right)\times\left[\coth\left(\frac{140.7}{T}\right)-0.8003\right] \\ \rho(T,\sigma) = 3.811\times10^{-6}+\left(-2.606\times10^{-10}\sigma+3.74\times10^{-7}\right)(T-16.06) \end{cases} \\ \text{TiZrHfCu}_{0.8}: \begin{cases} \varepsilon_r(T,\sigma) = \left(1.01\times10^6-\frac{4.935\times10^7}{1+2.7168\times10^{-10}f^2}\right)\left(1-8.191\times10^{-4}\sigma\right)\times\left[\coth\left(\frac{38.09}{T}\right)+1.9535\right] \\ \rho(T,\sigma) = 3.482\times10^{-6}+\left(-5.257\times10^{-11}\sigma+8.341\times10^{-8}\right)T \end{cases} \end{cases} \quad (36)$$

Thermal property tests reveal that the thermal conductivity α of both alloys increases with T, eventually stabilizing at 28.23 and 53.51 $W\cdot m^{-1}\cdot K^{-1}$, respectively, while the thermoelectric coefficient S is positively correlated with the heating rate. The thermal parameters can be expressed as:

$$\begin{cases} \text{TiZrHf}: \begin{cases} \kappa = 28.23-\frac{270.8}{T-14.55} \\ S = \left(6.877\times10^{-6}+1.501\times10^{-6}\frac{\partial T}{\partial t}\right) \end{cases} \\ \text{TiZrHfCu}_{0.8}: \begin{cases} \kappa = 53.51-\frac{77.08}{T-16.67} \\ S = \left(1.509\times10^{-5}+2.767\times10^{-6}\frac{\partial T}{\partial t}\right) \end{cases} \end{cases} \quad (37)$$

In this paper, the TiZrHf-based medium-entropy alloy is taken as the research object. Its thermo–mechano–electrical multi-physics coupling characteristics are systematically clarified, and the temperature- and stress-dependent mathematical expressions of multi-physical parameters are established. This work solves the core problem of the ambiguous

nonlinear coupling relationships among multi-physical parameters for such alloys under complex extreme environments. It can provide theoretical models and numerical simulation methods for the application of medium- and high-entropy alloys in the fields of impact-resistant protective armor, structural components for extreme environments, novel thermoelectric conversion materials, and stress/temperature coupling sensors.

This study is limited to temperatures $\leq$ 150 °C and stresses $\leq$ 900 MPa. Future work should extend to higher temperature regimes (on the order of 10^3 °C) and investigate cyclic/dynamic loading effects on the coupling behavior. Additionally, in situ microscopy under coupled fields could reveal underlying microstructural mechanisms.

Author Contributions: Conceptualization, E.T.; methodology, M.C.; software, C.C.; validation, B.W.; formal analysis, B.W.; investigation, B.W.; resources, E.T.; data curation, M.C.; writing—original draft preparation, M.C.; writing—review and editing, C.C.; visualization, B.W.; supervision, M.C.; project administration, E.T.; funding acquisition, M.C. All authors have read and agreed to the published version of the manuscript.

Funding: This research was funded by the Liaoning Talent Revitalization Program, grant number XLYC2403191.

Data Availability Statement: The original contributions presented in this study are included in the article material. Further inquiries can be directed to the corresponding author.

Acknowledgments: The authors are grateful to Kai Guo for her help with the processing of experimental data.

Conflicts of Interest: The authors declare no conflicts of interest.

Abbreviations

The following abbreviations are used in this manuscript:

BCC	Body-Centered Cubic
FCC	Face-Centered Cubic
AC	Alternating Current
DSC	Differential Scanning Calorimetry
SMA	Shape Memory Alloy
CBH	Correlated Barrier Hopping
NVAP	Non-Variable Amplitude Pulses
IVPA	Inhomogeneous Variable Amplitude Pulses
Φ	Diameter
H	Height
PI	Polyimide
T	Temperature
T_{h}	Temperature of the Heating Table
C	Capacitance
R	Resistance
LCR	Inductance-Capacitance-Resistance
σ	Stress
F	Pressure
S_s	Cross Section of Specimen
ε	Strain
ΔL	Change in Calibration Line Distance
L	Initial Distance Between Calibration Lines
R_{LCR}	Resistance Measured by LCR
R	Resistance of Specimen
R_0	Resistance of Air Domain

The relation between resistivity and resistance is

ρ_0	Resistivity of Air
ρ	Resistivity of Specimen
$H(\sigma)$	Stress-Related Height of Specimen
S_a	Cross-Sectional Areas of the Air
C_{LCR}	Capacitance Measured by LCR
C	Capacitance of Specimen
C_0	Capacitance of Air Domain
ε_0	Vacuum Dielectric Constant
ε_r	Relative Dielectric Constant of Specimens
f	Frequency
$\overline{T}$	Average Temperature
T_s	Stable Temperature
$\Delta\overline{T}$	Temperature Difference
U	Thermoelectric Voltage
$\Delta T/\Delta L$	Temperature Gradient
$\Delta T/\Delta t$	Heating Rate
A	Yield Strength
B	Strain Hardening Constant
n	Strain Hardening Exponent
ε_p	Plastic Strain
C	Strain Rate Strengthening Constant
$\dot{\varepsilon}_p$	Plastic Strain Rate
$\dot{\varepsilon}_0$	Reference Strain Rate
T_m	Melting Temperature
T_r	Reference Temperature
m	Temperature Softening Parameter
E	Elastic modulus
σ_{max}	Compression Strength
W_{Yeoh}	Strain Energy Function
I	First Invariants of Strain Tensor
σ_s	Yield Limit
ω_p	Resonance Frequency
τ	Relaxation Time of Electron
ω	Frequency of the Electromagnetic Wave
α_P	Initial Ferroelectric Expansion Coefficient
$T_q^{(P)}$	Quantum Vibration Temperature
$T_c^{(P)}$	"effective" Curie Temperature
$u(x,t)$	Temperature distribution
κ	Thermal Conductivity
S	Seebeck Coefficient
S_c	Constant part of S
k	Heating Rate Related Parameter

References

1. Stepanov, N.D.; Shaysultanov, D.G.; Salishchev, G.A.; Tikhonovsky, M.A. Structure and mechanical properties of a light-weight AlNbTiV high entropy alloy. *Mater. Lett.* **2015**, *142*, 153–155. [CrossRef]
2. Dong, Y.; Gao, X.; Lu, Y.; Wang, T.; Li, T. A multi-component $AlCrFe_2Ni_2$ alloy with excellent mechanical properties. *Mater. Lett.* **2016**, *169*, 62–64. [CrossRef]
3. Zhou, Y.; Jin, X.; Zhang, L.; Du, X.; Li, B. A hierarchical nanostructured $Fe_{34}Cr_{34}Ni_{14}Al_{14}Co_4$ high-entropy alloy with good compressive mechanical properties. *Mater. Sci. Eng. A* **2018**, *716*, 235–239. [CrossRef]
4. Song, J.F.; Chai, Z.S.; Zheng, J.; Wu, Q.; He, F.; Yang, Z.; Li, J.; Wang, J.; Yang, H.; Wang, Z. Design Fe-based Eutectic Medium-Entropy Alloys $Fe_2NiCrNb_x$. *Acta Metall. Sin.* **2021**, *34*, 1103–1108. [CrossRef]

5. Wang, Y.X.; Zhang, D.D.; Zhang, J.Y.; Liu, G.; Sun, J. Research Development of $CoCrFeNiNb_x$ High Entropy Alloys. *Rare Met. Mater. Eng.* **2022**, *51*, 743–751.
6. Wei, X.M.; Zhang, L.J.; Zhang, C.Z.; Li, G. A sunflower-like eutectic microstructure in the $AlCrFeMnNi_2$ high-entropy alloy with excellent compressive mechanical properties. *Mater. Lett.* **2023**, *339*, 134107. [CrossRef]
7. Zhang, C.; Xie, S.; Li, X.; Sun, R.; Liu, B.; Liu, W.; Yu, Q.; Xiong, H.; Zhang, R.; Yin, H. Revealing the mechanical behavior of Ti48-xZrxHf26Nb26 high-entropy alloy through zirconium content variations. *J. Alloys Compd.* **2024**, *992*, 174578. [CrossRef]
8. Qi, W.; Zhao, T.; Chen, R.; Wang, X.; Xu, Q.; Wang, S.; Fu, H. Collaborative optimization of microstructure, phase composition and room-temperature fracture toughness of Nb-Si based alloys using Ti, Zr and Hf elements. *Trans. Nonferrous Met. Soc. China* **2024**, *34*, 194–202.
9. Kannan, Y.B.; Saravanan, R.; Srinivasan, N.; Ismail, I. Effect of sintering on dielectric and AC conductivity properties of $Ni_{0.5}Zn_{0.5}Fe_2O_4$ nano ferrite particles. *J. Aust. Ceram. Soc.* **2017**, *53*, 577–581. [CrossRef]
10. Sharma, N.; Patial, B.S.; Thakur, N. On the Dielectric Study and AC Conductivity Measurements of Quaternary Se-Te-Ge-Pb Nano-chalcogenide Alloys. *J. Electron. Mater.* **2019**, *48*, 7089–7098. [CrossRef]
11. Kerli, S.; Alver, U.; Gögebakan, M. Investigation of the Electrical Properties of Al85Y9Ni6 Metallic Glass and Formulation of the Results. *Glass Phys. Chem.* **2020**, *46*, 189–193. [CrossRef]
12. Dagdelen, F.; Ozay, C.; Ercan, E.; Emir, G.; Qader, I.N. Change of electrical resistivity during phase transitions in NiMnSn-based shape memory alloy. *J. Therm. Anal. Calorim.* **2022**, *147*, 5815–5823. [CrossRef]
13. Ansari, R.; Gupta, D.; Kumar, H. Structural, dielectric and electrical properties of $Se_{96-x}Sn_4Sb_x$(x=0, 2, 4, 6, and 8) glassy alloys. *J. Alloys Compd.* **2023**, *936*, 168336. [CrossRef]
14. Chen, M.; Chang, M.; Li, Y.; Lin, X.; Chen, C.; Tang, E. Mechanism of electric-thermo-mechanical coupling response of TiZrHf medium-entropy alloy under impact loading. *J. Alloys Compd.* **2025**, *1030*, 180791. [CrossRef]
15. Yang, J.; Ma, Y.; Dong, P.; He, Y.; Ma, J.; Li, W.; Qu, Z. Theoretical model for predicting the yield strength of metal materials under electrically-assisted deformation. *Int. J. Heat Mass Transf.* **2025**, *238*, 126496. [CrossRef]
16. Ying, T.; Zheng, M.Y.; Li, Z.T.; Qiao, X.G.; Xu, S.W. Thermal conductivity of as-cast and as-extruded binary Mg-Zn alloys. *J. Alloys Compd.* **2015**, *621*, 250–255. [CrossRef]
17. Pan, H.C.; Huang, Y.M.; Gao, Z.Y.; Huang, Q.Y.; Peng, J.; Pan, F.S. Effect of Compounds Precipitation on Thermal Conductivity of Mg-Sn Binary Alloy. *Rare Met. Mater. Eng.* **2017**, *46*, 3311–3315.
18. Çadırlı, E.; Kaya, H.A.; Büyük, U.Ğ.; Şahin, M.; Üstün, E.; Gündüz, M. Investigation of the thermo-electrical properties of A707 alloys. *Thermochim. Acta* **2019**, *673*, 177–184. [CrossRef]
19. Ivanov, Y.; Levin, A.A.; Novikov, S.; Pshenay-Severin, D.; Volkov, M.; Zyuzin, A.; Burkov, A.; Nakama, T.; Schnatmann, L.; Reith, H.; et al. Low-temperature thermal conductivity of thermoelectric $Co_{1-x}M_xSi$(M = Fe, Ni) alloys. *Mater. Today Energy* **2021**, *20*, 100666. [CrossRef]
20. Chen, L.; Lu, S.L.; Guo, W.; Li, J.; Wu, S. High thermal conductivity of highly alloyed Mg-Zn-Cu alloy and its mechanism. *J. Alloys Compd.* **2022**, *918*, 165614. [CrossRef]
21. Liu, X.; Chang, L.; Ma, T.; Zhou, C. Molecular dynamics simulation of tension and compression deformation behavior in CoCrCuFeNi high-entropy alloy: Effects of temperature and orientation. *Mater. Today Commun.* **2023**, *36*, 106523. [CrossRef]
22. Liu, J. Molecular dynamic study of temperature dependence of mechanical properties and plastic inception of CoCrCuFeNi high-entropy alloy. *Phys. Lett. A* **2020**, *384*, 126516. [CrossRef]
23. Kuang, X.J. Discussion on dielectric constant of metal. *J. Sichuan Univ. Sci. Eng.* **2006**, *19*, 75–78.
24. Uporov, S.A.; Evdokimov, I.V.; Sidorov, V.A.; Chtchelkatchev, N.M.; Bykov, V.A.; Sterkhov, E.V.; Balyakin, I.A.; Ryltsev, R.E. Superior strain gauge sensitivity and elastic anisotropy in TiZrHfTa high entropy alloy. *Intermetallics* **2025**, *177*, 108575. [CrossRef]
25. Uporov, S.A.; Ryltsev, R.E.; Sidorov, V.A.; Estemirova, S.K.; Sterkhov, E.V.; Balyakin, I.A.; Chtchelkatchev, N.M. Pressure effects on electronic structure and electrical conductivity of TiZrHfNb high-entropy alloy. *Intermetallics* **2022**, *140*, 107394. [CrossRef]

Disclaimer/Publisher's Note: The statements, opinions and data contained in all publications are solely those of the individual author(s) and contributor(s) and not of MDPI and/or the editor(s). MDPI and/or the editor(s) disclaim responsibility for any injury to people or property resulting from any ideas, methods, instructions or products referred to in the content.